

Source estimation and rock physics preconditioning for anisotropic full waveform inversion

Huy Le, Biondo Biondi, Robert G. Clapp, Stewart A. Levin, and Tapan Mukerji

ABSTRACT

In the imaging and inversion of long-offset seismic data, it is necessary to incorporate anisotropy to produce accurate images and subsurface models. Building an anisotropic model is a challenging inverse problem because of the large number of unknown parameters. To reduce the number of unknown parameters, it is common to assume a simple physics, for example, using the acoustic approximation or constant density. This leads to a mismatch in amplitude between the modeled data and the observed data. Estimation of the source wavelet by directly minimizing the inversion's objective function can help to mitigate this mismatch. Adding to the challenge of anisotropic model building is the fact that anisotropic parameters are often of different types, such as velocity, stiffness, or Thomsen's parameters. Consequently, one needs to account for their crosstalk and sensitivity. We follow an established workflow that stochastically simulates these parameters based on rock physics and compaction models. This simulation provides information about the model covariance, which can be used to reduce parameter crosstalk.

INTRODUCTION

The acquisition of long-offset three dimensional seismic data often requires imaging and inversion algorithms to go beyond isotropy. The simplest anisotropic model is transverse isotropy, which has one axis of rotational symmetry, i.e. seismic wave velocity depends on the angle between propagation direction and symmetry axis. This type of anisotropy is commonly found in layered media and shale reservoirs.

To fully describe a transverse isotropic medium, we need six parameters, including five stiffnesses and one density. In the context of waveform inversion and model building, it is hardly possible to estimate that many number of parameters. As a result, the industry commonly uses approximations, for example, constant density and acoustic media. For anisotropy, the resulting wave equations from such approximations were derived by Alkhalifah (2000) and are usually referred to as pseudo-acoustic.

The pseudo-acoustic anisotropic wave equations have been widely used and demonstrated to accurately capture the kinematics of seismic waves (Fletcher et al., 2009;

Zhang et al., 2011; Bube et al., 2012; Warner et al., 2013). The assumptions of constant density and acoustic media can lead to an amplitude mismatch between the simulated data and the observed data, which can be harmful in waveform inversion. One approach to reduce this mismatch is to directly estimate the source wavelet by minimizing the objective function. In this paper, we derive a method to estimate the source wavelet using the pseudo-acoustic wave equations in anisotropic media.

The second half of this paper deals with the problem of crosstalk and sensitivity among different anisotropic parameters. We adopt a workflow introduced by Bachrach (2010) that stochastically models anisotropic parameters using rock physics and compaction trends of sand and shale. In this workflow, sand’s mineral matrix is modeled with quartz while shale’s matrix is modeled as a composition of smectite and illite. Both sand’s pore and shale’s pore are brine-filled. Temperature is used as an indication of volumes fractions of smectite and illite, i.e. the higher the temperature, the greater the illite fraction (Freed and Peacor, 1989). Anisotropy of shale is determined by compaction, as clay minerals align, via porosity. A similar workflow has been incorporated successfully to wave equation migration velocity analysis (Li et al., 2016). We here extend it to full waveform inversion (FWI).

SOURCE INVERSION

Derivation

Using the second-order pseudo acoustic anisotropic wave equations, Le (2016) derived adjoint equations and recursive relations to compute the derivatives of the FWI objective function with respect to model parameters. To estimate the source, $s(t)$, we minimize the same objective function as when inverting for velocity models, \mathbf{m} , i.e. the l_2 -norm of the different between the modeled, d and the observed data, d_0 :

$$f(\mathbf{m}, s) = \frac{1}{2} \|d(\mathbf{x}_r, t; \mathbf{m}, s) - d_0(\mathbf{x}_r, t)\|_2^2. \quad (1)$$

Since the wave equations are linear differential equations, so is the modeled data with respect to the source function:

$$d = \mathbf{R}\mathbf{P}\mathbf{Q}s, \quad (2)$$

where:

- \mathbf{Q} is the injection of the source function at shot locations,
- \mathbf{P} is the forward propagation operator,
- and \mathbf{R} is the recording of wavefields at receivers.

The linear relationship between the modeled data and the source function makes our objective function quadratic, whose minima can be reached using methods like

conjugate gradient if we iterate long enough, i.e. equal to number of source function samples.

The gradient of the objective function 1 can be easily computed:

$$\frac{\partial f}{\partial s} = \mathbf{Q}^T \mathbf{P}^T \mathbf{R}^T (d - d_0), \quad (3)$$

where:

- \mathbf{R}^T is the injection of receiver locations,
- \mathbf{P}^T is the backward propagation operator,
- and \mathbf{Q}^T is the recording at source locations.

Synthetic example

We perform a synthetic test of source inversion on the BP 2007 models. Figure 1 shows the true models that are used to create the synthetic observed data and Figure 2 shows the smooth background models used in the inversion. Sources and receivers are placed on the surface. We used a band-limited wavelet from a real airgun signature as an input. Figure 3 shows the inversion results. The inverted wavelet matches the input wavelet really well, both in terms of waveform (Figure 3a) and frequency amplitude (Figure 3b). The inverted wavelet, however, shows some high-frequency ringing noise that can be observed in its waveform and spectrum at about 50 and 70 Hz. This is due to the band-limited nature of the input wavelet that high-frequency noise leaks in from the null space. The objective function reduced 95% after only 14 iterations (Figure 3c).

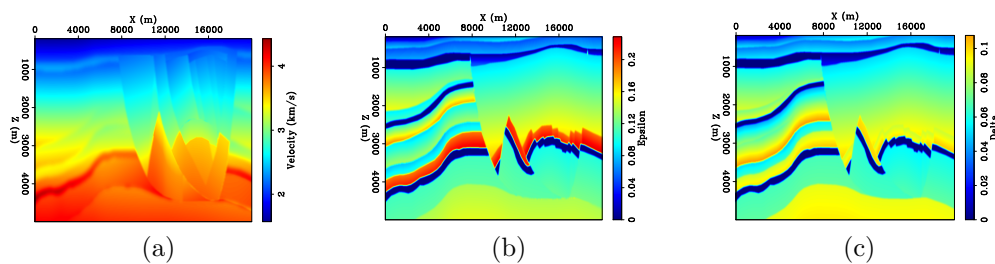


Figure 1: True models used to generate synthetic observed data: (a) vertical velocity in km/s, (b) ϵ , and (c) δ . [ER]

ROCK PHYSICS TO PRECONDITION FWI

To deal with the problem of parameter crosstalk in anisotropic FWI, one approach is to incorporate additional information, such as well logs or seismic attributes, to

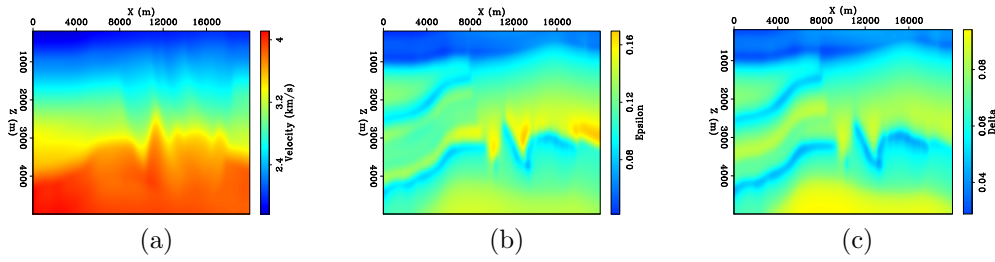


Figure 2: Smooth background models used in the inversion: (a) vertical velocity in km/s, (b) ϵ , and (c) δ . [ER]

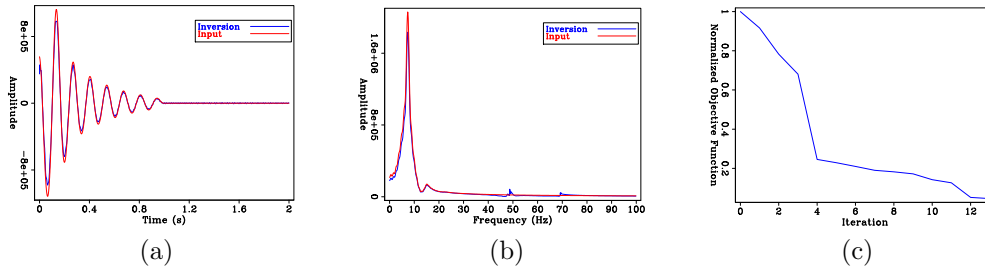


Figure 3: Inversion results: (a) input (red) and inverted (blue) wavelets, (b) spectra of input (red) and inverted (blue) wavelet, and (c) objective function reduction with iterations. [CR]

constrain the inversion. Particularly, combining with rock physics and compaction models, one can sample the model space of anisotropic parameters. This sampling provides us with covariance information of model parameters, which can be used as a preconditioner to separate the crosstalk. Bachrach (2010) presented a workflow that stochastically simulates anisotropic models using rock physics principles of shale compaction and anisotropy described in Bandyopadhyay (2009). We extend this workflow to model a sand-shale layered medium.

Inputs

Our rock physics workflow requires subsurface temperature and shale volume as direct inputs. Temperature controls the transition from smectite to illite, which are the two clay minerals that compose shale (Bachrach, 2010):

$$P_{\text{illite}}(T) = \frac{1}{2} + \frac{1}{2} \tanh \left(\frac{T - T_T}{2s_T} \right). \quad (4)$$

Here P_{illite} is the percentage of illite, T_T is the transition temperature, where 50% of the smectite-illite reaction has occurred, and s_T is the spread of the transition (Freed and Peacor, 1989).

While temperature can be obtained from basin modeling using borehole data or by assuming a constant depth gradient, shale volume is an attribute that can be obtained

from seismic inversion and rock physics transforms. Besides these two direct inputs, it is critical to have well logs, such as gamma ray, sonic logs, and density, for the calibration of rock physics model parameters.

Compaction model

Compaction influences physical properties of rocks, such as porosity and anisotropy. Here we use a normal compaction trend that is commonly adopted for porosity of water-saturated sand and shale in the Gulf of Mexico (Dutta et al., 2009):

$$\phi = ae^{bz} + ce^{dz}. \quad (5)$$

In sand, porosity directly affects density and stiffness of rocks. In shale, compaction determines the alignment of clay minerals, which controls the degree of anisotropy. The more a shale rock is compacted, the more aligned its clay minerals are, and therefore the more anisotropic it is. This relation makes stiffnesses of clay in the subsurface different from those of a single clay mineral. Sayers (1994) derived equations for anisotropy of shale as functions of its orientation distribution:

$$\begin{aligned} c_{11} &= \lambda + 2\mu + \frac{4\sqrt{2}}{105}\pi^2(2\sqrt{5}a_3W_{200} + 3a_1W_{400}), \\ c_{33} &= \lambda + 2\mu - \frac{16\sqrt{2}}{105}\pi^2(\sqrt{5}a_3W_{200} - 2a_1W_{400}), \\ c_{44} &= \mu - \frac{2\sqrt{2}}{315}\pi^2 \left[\sqrt{5}(7a_2 + a_3)W_{200} + 24a_1W_{400} \right], \\ c_{12} &= \lambda - \frac{4\sqrt{2}}{315}\pi^2 \left[2\sqrt{5}(7a_2 - a_3)W_{200} - 3a_1W_{400} \right], \\ c_{13} &= \lambda + \frac{4\sqrt{2}}{315}\pi^2 \left[\sqrt{5}(7a_2 - a_3)W_{200} - 12a_1W_{400} \right], \end{aligned} \quad (6)$$

where:

$$\begin{aligned} a_1 &= c_{11}^a + c_{33}^a - 2c_{13}^a - 4c_{44}^a, \\ a_2 &= c_{11}^a - 3c_{12}^a + 2c_{13}^a - 2c_{44}^a, \\ a_3 &= 4c_{11}^a - 3c_{33}^a - c_{13}^a - 2c_{44}^a, \\ \lambda &= \frac{1}{15}(c_{11}^a + c_{33}^a + 5c_{12}^a + 8c_{13}^a - 4c_{44}^a), \\ \mu &= \frac{1}{30}(7c_{11}^a + 2c_{33}^a - 5c_{12}^a - 4c_{13}^a + 12c_{44}^a). \end{aligned} \quad (7)$$

In the above equations, c_{ij}^a are the stiffnesses of a domain, i.e. a single clay mineral, either smectite or illite, and c_{ij} are the averaged stiffnesses of aligned clay particles. W_{200} and W_{400} are the orientation distribution parameters and related to compaction

via porosity (Bachrach, 2011):

$$\begin{aligned} W_{200}(\phi) &= W_{200}^{\max} \left(1 - \frac{\phi}{\phi_0}\right)^m, \\ W_{400}(\phi) &= W_{400}^{\max} \left(1 - \frac{\phi}{\phi_0}\right)^n, \end{aligned} \quad (8)$$

where $W_{200}^{\max} = \frac{\sqrt{2.5}}{4\pi^2}$ and $W_{400}^{\max} = \frac{\sqrt{4.5}}{4\pi^2}$ are the maxima of W_{200} and W_{400} respectively, when clay particles are completely aligned, m and n are empirical parameters, and ϕ_0 is the critical porosity, i.e. the porosity above which mineral grains are no longer in contact but suspended in the fluid.

Rock physics model

We model a rock as composed of layers of sand and shale. When porosity is less than critical porosity, to model sand, we use the Differential Effective Medium (DEM) equations with water-filled inclusion in quartz background (Hornby et al., 1994). Modeling shale follows a similar procedure as does sand, except that the background mineral is now clay instead of quartz. Elastic properities of clay are computed as Backus's average of smectite and illite (Backus, 1962):

$$\begin{aligned} C_{11}^{\text{clay}} &= \langle \frac{c_{13}}{c_{33}} \rangle^2 \langle \frac{1}{c_{33}} \rangle^{-1} - \langle \frac{c_{13}^2}{c_{33}} \rangle + \langle c_{11} \rangle, \\ C_{12}^{\text{clay}} &= C_{11}^{\text{clay}} - \langle c_{11} \rangle + \langle c_{12} \rangle, \\ C_{13}^{\text{clay}} &= \langle \frac{c_{13}}{c_{33}} \rangle^2 \langle \frac{1}{c_{33}} \rangle^{-1}, \\ C_{33}^{\text{clay}} &= \langle \frac{1}{c_{33}} \rangle^{-1}, \\ C_{44}^{\text{clay}} &= \langle \frac{1}{c_{44}} \rangle^{-1}, \end{aligned} \quad (9)$$

where c_{ij} are stiffnesses of smectite and illite computed from Equations 6 and $\langle \cdot \rangle$ stands for the average of the enclosed quantity weighted by their volume fractions. After modeling sand and shale separately, we use Backus's average again to obtain the elastic stiffnesses of our sand-shale rock layers.

When porosity is greater than critical porosity, we use Reuss average of water and the mineral matrix:

$$\frac{1}{C_{ij}} = \frac{1 - \phi}{C_{ij}^{\text{matrix}}} + \frac{\phi}{C_{ij}^{\text{water}}}. \quad (10)$$

One important parameter, and input to DEM, is the pore aspect ratio. In our workflow, we choose to model pores with elliptical shapes and define aspect ratio as the ratio between the vertical axis and the horizontal axis. An aspect ratio of one,

i.e. spherical pores, would result in a hard and isotropic rock, if the background matrix is also isotropic. Under compaction and deposition, however, pores tend to be deformed and elongated horizontally, resulting in an anisotropic rock that is soft in the z-direction but harder in the x-direction. Bandyopadhyay (2009) defined aspect ratio as a function of porosity:

$$a = \frac{(1 - \phi_0)\phi}{(1 - \phi)\phi_0}. \quad (11)$$

In reality, not all pores are deformed and oriented in the same direction, so we use Equation 11 to model aspect ratio for half of the pores and choose random aspect ratios for the other half.

Stochastic rock physics modeling workflow

Many parameters in the above workflow are either not certainly determined, well studied, empirical, or theoretical, such as smectite-illite reaction temperature parameters, T_T and s_T (Equation 4), critical porosity, ϕ_0 , exponent parameters, m and n (Equation 8), or pore aspect ratio (used in DEM). We can account for this uncertainty and explore the model space by varying these parameters within some ranges and simulating a number of realizations of subsurface anisotropic models. The means and covariances of these models can be used to constrain anisotropic FWI. We summarize the rock physics workflow in the following:

1. From uniform distributions, randomly select values for parameters like reaction temperatures, T_T and s_T (Equation 4), exponent parameters, m and n (Equations 8), and aspect ratio. Tables 1 and 2 show values and ranges of parameters used in our workflow.
2. Compute porosity for sand and shale (Equation 5) and the total porosity.
3. Model sand and shale using either DEM or Reuss average depending on porosity.
4. Compute the average stiffnesses of sand-shale layers using Backus's average (Equations 9).
5. Compute the mean models and covariances.

Choosing the ranges of the input parameters into our workflow is also an important task. Here is where the well data come in handy. The above simulation is usually performed several times and the input parameters are tuned so that the outputs match well data.

Mineral	ρ (kg/m ³)	v_p (m/s)	v_s (m/s)	ϵ	δ	γ
Quartz	2650	6000	4000	0	0	0
Smectite	2400	3250	1500	0.1	0.05	0.18
Illite	2600	4250	2519	0.2	0.1	0.28

Table 1: Mineral properties used in our study based on Bachrach (2011).

Parameter	Value/range
Critical porosity ϕ_0	0.45
Thermal gradient	2.13° C/100 m
Transition temperature T_T	60-90° C
Transition spread s_T	40-80° C
Exponents n and m	0.5-2
Aspect ratio a	0.5-1.5

Table 2: Values and ranges of parameters used in our study. Value for thermal gradient is taken from Forrest et al. (2005). Ranges for smectite-illite transition temperature and spread are based on Freed and Peacor (1989). Ranges for exponents n and m are from Bachrach (2010).

ROCK PHYSICS MODELING ON A FIELD DATA

We apply the above described workflow to a field data collected in the Gulf of Mexico (courtesy of WesterGeco). Figure 4a shows the porosity-depth trends for sand and shale (Equations 5). Note that shale’s porosity decreases much faster with depth than sand’s porosity. Figures 4b and 4c show the shale volume and the total porosity. Figure 5 shows the mean velocity, ϵ , and δ . These mean models share similar structures with the shale’s volume (4b). Anisotropy generally increases with depth, as we expect.

Figure 6a compares the probability density functions (PDF) of velocity from our rock physics simulation and well data. The simulated PDF does not match the data well. Particularly our simulation does not capture velocity range from 1600-2500 m/s. We anticipate this is because of the abrupt transition from unconsolidated rocks near the water bottom (porosity greater than critical porosity) to consolidated rocks (porosity lower than critical porosity). Figures 6b and 6c show the simulated PDFs of ϵ and δ . One noticeable feature among these simulated PDFs is that they are all trimodal.

Figure 7 shows the model variances. Notice that velocity variance is much greater than those of ϵ and δ . For all three parameters, variances increase with depth. It is more interesting to observe that velocity has negative correlations with Thomsen’s parameters, indicated by negative covariances between velocity and ϵ (Figure 8a) and between velocity and δ (Figure 8c). The two Thomsen’s parameters, on the other hand, are positively correlated (Figure 8b). Note that we only compute these model

variances and covariances at individual locations, and therefore, do not capture any spatial correlation information. Nevertheless, these covariances can still be used as preconditioners for FWI to separate crosstalk among parameters.

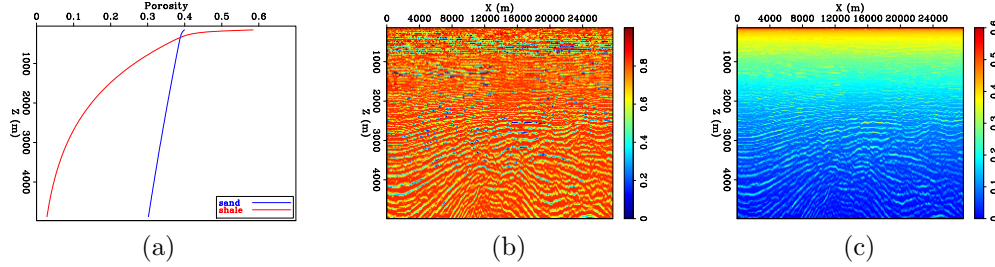


Figure 4: (a) Porosity-depth trends for sand and shale; (b) Provided shale volume (courtesy of WesternGeco); (c) Total porosity. [CR]

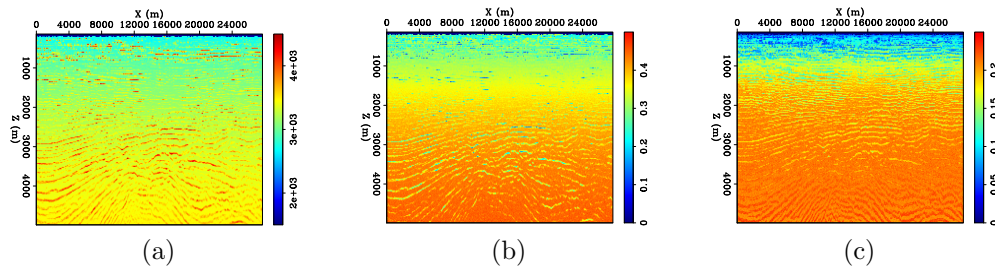


Figure 5: Mean models of: (a) velocity, (b) ϵ , and (c) δ [CR]

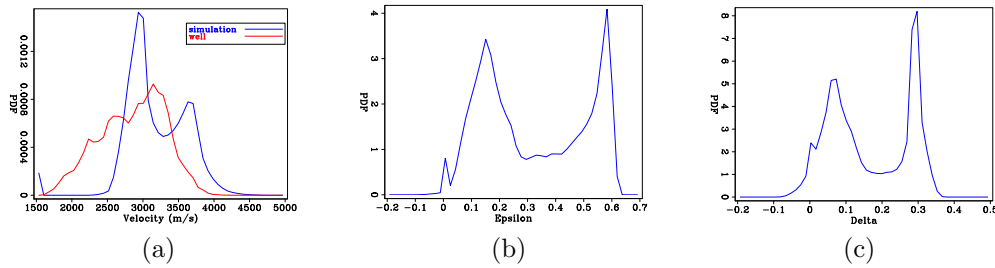
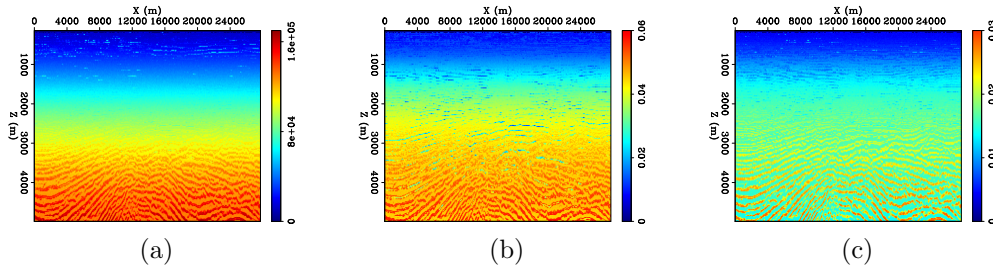
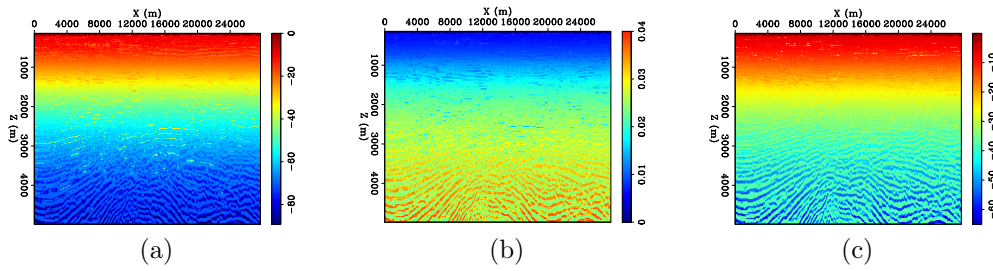


Figure 6: Probability density functions (PDF) of: (a) velocity (including data supplied by IHS Energy Log Services, Copyright 2017, IHS Energy Log Services Inc.), (b) ϵ , and (c) δ [CR]

CONCLUSIONS

In this report, we present two different approaches to improve anisotropic FWI. The first approach is to estimate the source wavelet directly from the observed data by minimizing the FWI objective function. This is particularly helpful to mitigate any amplitude difference between the modeled data and the observed data, caused by assumptions and approximations in the modeling engine. A simple synthetic example

Figure 7: Variances of : (a) velocity, (b) ϵ , and (c) δ [CR]Figure 8: Covariances of : (a) velocity and ϵ , (b) ϵ and δ , and (c) velocity and δ [CR]

validates our implementation of source wavelet inversion. More complicated tests are to be carried out to evaluate how source estimation could improve FWI.

The second approach is to use rock physics modeling to estimate model covariances and preconditioners. We present a workflow that models sand-shale layers using Reuss average for unconsolidated rocks and Differential Effective Medium theory for consolidated rocks. The model covariances are computed by varying parameters such as smectite-illite transition temperatures, pore aspect ratio, and compaction factors. stochastically simulating many anisotropic earth models. Our application on a field data, however, does not produce satisfactory results. In particular, our simulated probability density function of velocity does not match well data. We suspect that the density function mismatch might be due to the sharp transition from unconsolidated rocks to consolidated rocks that is not captured well by Reuss average and Differential Effective Medium theory. This also signifies the importance of data calibration in order to correctly describe model parameters' statistics.

ACKNOWLEDGEMENTS

We would like to thank WesternGeco for their donation of the shale volume and IHS Energy Log Services Inc. for the well logs. We also would like to thank Iris Yang from the Stanford Rock Physics group for providing the DEM codes.

REFERENCES

- Alkhalifah, T., 2000, An acoustic wave equation for anisotropic media: *Geophysics*, **65**, 1239–1250.
- Bachrach, R., 2010, Applications of deterministic and stochastic rock physics modeling to anisotropic velocity model building: SEG Annual International Meeting, Expanded Abstracts, 2436–2440, Society of Exploration Geophysicists.
- , 2011, Elastic and resistivity anisotropy of shale during compaction and diagenesis: Joint effective medium and field observations: *Geophysics*, **76**, No. 6, E175–E186.
- Backus, G. E., 1962, Long-wave elastic anisotropy of horizontal layering: *Journal of Geophysical Research*, **67**, 4427–4440.
- Bandyopadhyay, K., 2009, Seismic anisotropy: Geological causes and its implications to reservoir geophysics: PhD thesis, Stanford University.
- Bube, K. P., T. Nemeth, J. P. Stefani, R. Ergas, W. Liu, K. T. Nihei, and L. Zhang, 2012, On the instability in second-order systems for acoustic VTI and TTI media: *Geophysics*, **77**, No. 5, T171–T186.
- Dutta, T., G. Mavko, T. Mukerji, and T. Lane, 2009, Compaction trends for shale and clean sandstone in shallow sediments, Gulf of Mexico: *The Leading Edge*, **28**, 590–596.
- Fletcher, R. P., X. Du, and P. J. Fowler, 2009, Reverse time migration in tilted transversely isotropic (TTI) media: *Geophysics*, **74**, No. 6, WCA179–WCA187.
- Forrest, J., E. Marcucci, and P. Scott, 2005, Geothermal gradients and subsurface temperatures in northern Gulf of Mexico: *GCAGS Transactions*, **55**, 233–248.
- Freed, R. L. and D. R. Peacor, 1989, Variability in temperature of the smectite/illite reaction in gulf coast sediments: *Clay Minerals*, **24**, 171–180.
- Hornby, B. E., L. M. Schwartz, and J. A. Hudson, 1994, Anisotropic effective medium modeling of the elastic properties of shales: *Geophysics*, **59**, 1570–1583.
- Le, H., 2016, Anisotropic full waveform inversion : SEP-Report, **163**, 155–162.
- Li, Y., B. Biondi, R. Clapp, and D. Nichols, 2016, Integrated VTI model building with seismic data, geological information, and rock-physics modeling-Part 1: Theory and synthetic test: *Geophysics*, **81**, C177–C191.
- Sayers, C. M., 1994, The elastic anisotropy of shale: *Journal of Geophysical Research*, **99**, 767–774.
- Warner, M., A. Ratcliffe, T. Nangoo, J. Morgan, A. Umpleby, N. Shah, V. Vinje, I. Stekl, L. Guasch, C. Win, G. Conroy, and A. Bertrand, 2013, Anisotropic 3D full-waveform inversion: *Geophysics*, **78**, No. 2, R59–R80.
- Zhang, Y., H. Zhang, and G. Zhang, 2011, A stable TTI reverse time migration and its implementation: *Geophysics*, **76**, No. 3, WA3–WA11.